Steel and Composite Structures, *Vol. 34, No. 1* (*2020*) *107-122*
DOI: https://doi.org/10.12989/scs.2020.34.1.107

Development and testing of cored moment resisting stub column dampers

Po-Chien Hsiao*[1], Kun-Sian Lin[2], Wei-Chieh Liao[2],
Limeng Zhu[3] and Chunwei Zhang[3]

[1]Department of Civil and Construction Engineering, National Taiwan University of Science and Technology, 43 Keelung Rd., Sec.4, Taipei City 106, Taiwan
[2]Department of Civil Engineering, National Chung Hsing University, 145 Xingda Rd., South Dist., Taichung City 402, Taiwan
[3]School of Civil Engineering, Qingdao University of Technology, 11 Fushun Rd., Shibei Dist., Qingdao, 266033, P.R. China

(*Received April 14, 2019, Revised November 11, 2019, Accepted November 30, 2019*)

Abstract. Moment resisting stub columns (MRSCs) have increasingly adopted in special moment-resisting frame (SMF) systems in steel building structures, especially in Asian countries. The MRSCs typically provide a lower deformation capacity compared to shear-panel stub columns, a limited post-yield stiffness, and severe strength degradation as adopting slender webs. A new MRSC design with cored configuration, consisting of a core-segment and two side-segments using different steel grades, has been proposed in the study to improve the demerits mentioned above. Several full-scale components of the cored MRSC were experimentally investigated focusing on the hysteretic performance of plastic hinges at the ends. The effects of the depths of the core-segment and the adopted reduced column section details on the hysteretic behavior of the components were examined. The measured hysteretic responses verified that the cored MRSC enabled to provide early yielding, great ductility and energy dissipation, enhanced post-yield stiffness and limited strength degradation due to local buckling of flanges. A parametric study upon the dimensions of the cored MRSC was then conducted using numerical discrete model validated by the measured responses. Finally, a set of model equations were established based on the results of the parametric analysis to accurately estimate strength backbone curves of the cored MRSCs under increasing-amplitude cyclic loadings.

Keywords: stub columns; moment resisting frames; post-yield stiffness; reduced column sections

1. Introduction

Special moment-resisting frame (SMF) have been commonly used as a seismic load resisting system in building structures all around the world. The SMF provides a relatively flexible behavior compared to braced or shear-wall frame systems, and therefore it is usually adopted to combine with various types of damper devices to effectively improve its seismic performance and reduce seismic responses, such as by increasing overall stiffness, strength or energy dissipation (damping) of the system. Adopting stub columns (SCs) in the SMF provides an alternative solution to stiffen and strengthen the buildings to meet the deformation requirements per current design code with many benefits, such as to increase overall stiffness and strength, and to limit the impact on architectural versatility in the building. Fig. 1 gives a typical example of real applications of SCs in SMF systems in Taiwan. The SCs are column-like members attaching top and bottom girders at mid-span of the bay where the SCs are installed, and mainly adopted to resist seismic loads rather than gravity loads. It should be noted that the configuration of the SC does not block out entire space in the bay yet remains sufficient architectural versatility. The applications of adopting SCs in the SMF system becomes more and more popular in the current practice compared with applications using brace- or wall-type members, especially in many Asia countries. It should be noted that the installed SCs would introduce additional moment and shear forces to the surrounding beams, therefore, they are typically arranged around the mid-span to avoid the impact on the functionality of plastic hinges at the ends of the beams. For high-rise buildings, the SCs would result in considerable axial loads due to the accumulation of gravity loads of stories above, which might significantly affect seismic performance of the SCs, therefore, certain detailing or strategy to release the axial loads of SCs is needed in the design.

Various design details of SCs have been developed to achieve ductility and sufficient energy dissipation. They can be categorized into two types, including shear panel and moment-resisting types (Fig. 2). The shear panels used in SCs behave similar with vertical shear links in eccentrically braced frames (EBFs) or other steel structures (Lian *et al*. 2019, Zahrai 2015, Shayanfar *et al*. 2012). It utilizes plasticity of steel panel, which is typically arranged in the middle portion of the SC to form a shear plastic hinge, as shown in Fig. 2, referred to as shear panel stub column (SPSC). Low yield steel plates were usually adopted for the shear panel with proper boundary plates and transverse stiffeners to achieve early yielding and large ductility (Soltani *et al*. 2017, Nakashima 1995). Many other design details of SPSC have been developed for various applications in the building structures. Shear penal without

*Corresponding author, Assistant Professor
E-mail: pchsiao@mail.ntust.edu.tw

http://www.techno-press.org/?journal=scs&subpage=6 ISSN: 1229-9367 (Print), 1598-6233 (Online)

Fig. 1 A real application of SCs in a SMF building structure

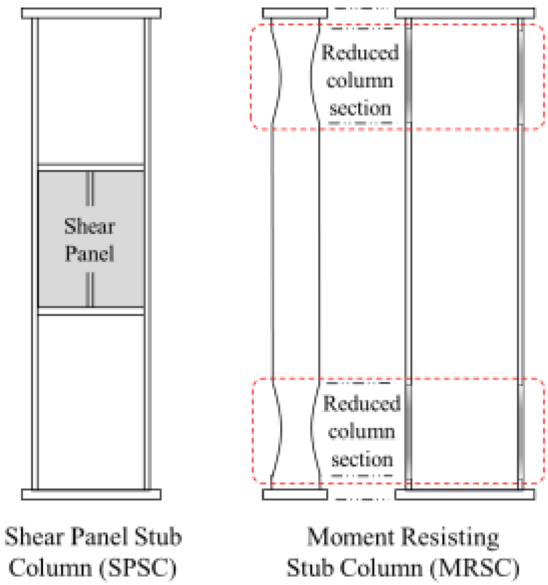

Fig. 2 Two types of stub columns

boundary plates yet with buckling restrained components was developed and verified to provide ductile hysteretic behavior (Deng *et al*. 2015). Kim *et al*. (2017) adopted the steel plate slit dampers for the applications of structural retrofitting. He *et al.* (2015) proposed a design of shear panels with tapered-link details to provide a stable hysteric behavior along with a feature of story drifts monitoring.

Instead of forming shear plastic hinge in SCs, reduced column sections (RCSs) are commonly adopted in SCs to form moment plastic hinges at the ends of SCs as shown in Fig. 2, and the SC is referred to as moment resisting stub column (MRSC). The detailing of the end connections of MRSC should conform to that of fully restrained (FR) moment connections specified for beam-column joints in MRFs (Tsai *et al.* 1995) to ensure the formation of plastic hinges without premature failure. The details of reduced column/beam sections have been experimental verified to effectively shift plastic regions away from beam-column joints to avoid brittle failure at joints (Lu *et al.* 2018, Zahrai *et al*. 2017, Jones *et al*. 2002, Uang and Fan 2001). However, the previous experimental results show that the beam-column joints with reduced beam section connections presented high strength degradation beyond plastic hinge formation and thereby reduced ductility when the web slenderness ratio is high (Lu *et al.* 2018, Jones *et al*. 2002, Uang and Fan 2001). Similar results were also observed for the cyclic performance of deep and built-up columns (Dehghan *et al.* 2018, Elkady and Lignos 2015, Alfreddo *et al.* 2014). Moreover, MRSCs perform similar with long links (i.e., moment control links) in EBFs yet arranged vertically in the frame. Previous research has verified that long links provide much lower rotational capacity compared

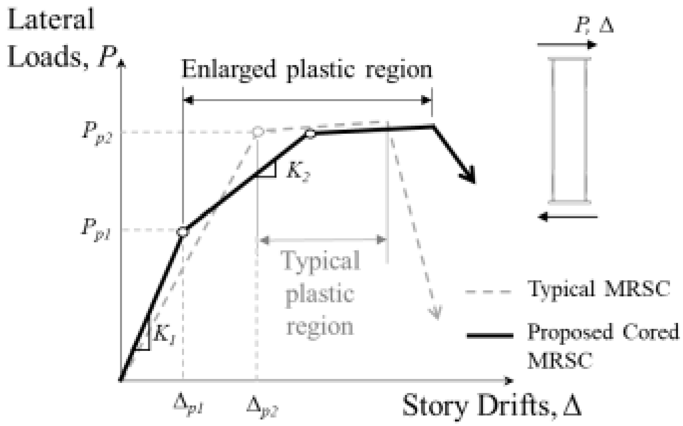

Fig. 3 Strength backbone curves of hysteretic behaviors of typical and proposed cored MRSCs

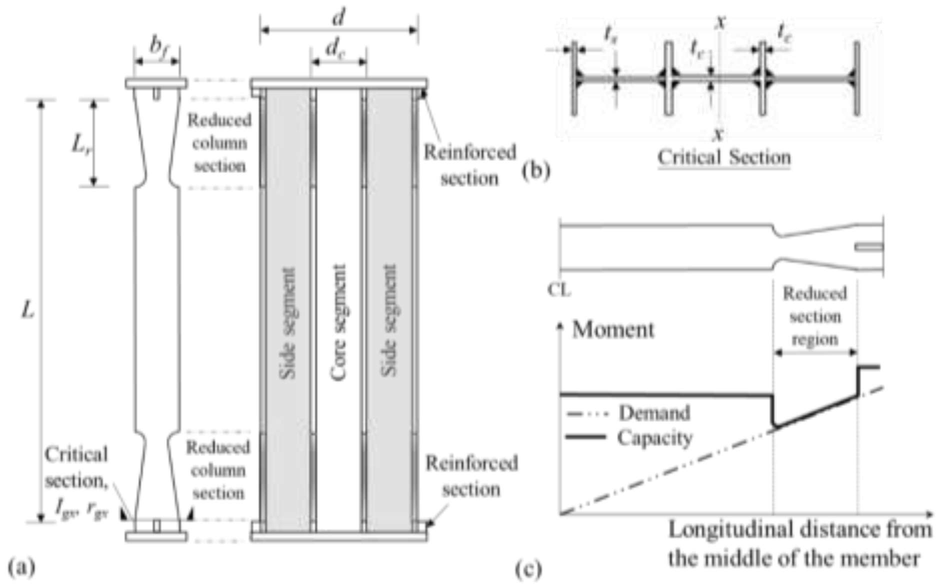

Fig. 4 Illustration of (a) the proposed cored MRSC, (b) cross section of the critical section, and (c) the detailing of RCSs

to shear links (Richards and Uang 2005, Engelhardt and Popov 1992). The typical MRSC with medium-to-large strength capacity potentially requires large web slenderness ratio which potentially leads to severe strength degradation beyond the formation of plastic hinge and reduced ductility as illustrated in Fig. 3. Furthermore, both of SPSC with shear plastic hinges and MRSC with moment plastic hinges provide very limited post-yield stiffness. Greater post-yield stiffness of structural systems was found to benefit the reduction of seismic responses of structural systems beyond the formation of plastic hinges (Ye *et al.* 2008, Hsiao and Liao 2019).

To improve the drawbacks mentioned above, the study developed an alternative design of MRSC with a cored configuration which is referred to as cored MRSC hereinafter, as illustrate in Figs. 4. The design consists of a) a combination of core- and side-segments using different steel grades (Figs. 4(a) and 4(b)), and b) detailing of RCSs (Fig. 4(c)) to achieve a ductile hysteretic behavior having (1) earlier energy dissipation, (2) enhanced post-yielding stiffness, (3) improved ductility and (4) postponed and mitigated the strength degradation beyond the formation of plastic hinges compared to the typical MRSCs, as illustrated in Fig. 3. In the study, the pilot tests of the cored MRSCs was conducted. An associated numerical model was then established to accurately simulate experimental responses prior to be adopted for a parametric study. Regression analysis was performed based on the results of the parametric study, and a set of general equations were then established to estimate the strength backbone curves of the proposed cored MRSCs, including yield strength, initial and post-yield stiffness of the member against some non-dimensional geometric parameters.

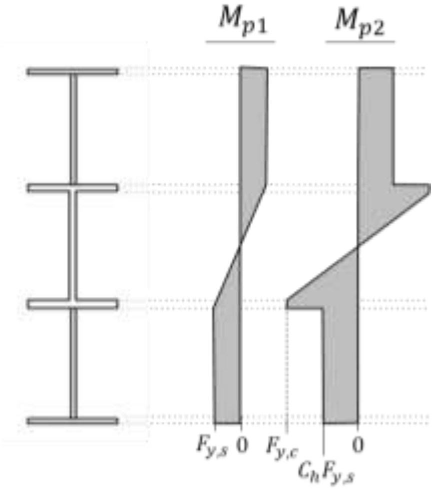

Fig. 5 Estimation of two-phase plastic moment capacities of cored MRSCs

2. Design and basic mechanism of the cored MRSCs

The cored MRSC was composed of one built-up wide-flange section (H-section) core-segment and two built-up wide-flange-tee section (T-section) side-segments, as illustrated in Fig. 4(b). The side-segments were arranged on the sides of the member using relatively low yield steel to form early yielding behavior and energy dissipation, while the core-segment was arranged in the middle using relatively high strength steel to delay the formation of plasticity. The core-segment was aimed to mainly remain elastic without flange local buckling to enhance hysteretic stability and overall post-yield stiffness beyond the yielding of the side-segments, as illustrated in Fig. 3. The core-segment arranged in the middle and having relatively small depth, d_c, tended to have lower strain deformation demands on the flanges and thereby would yield at a relatively large drift level, Δ_{p2}, as shown in the figure. In this configuration, the web slenderness ratio of the member was significantly reduced since the presence of the core-segment and thereby mitigate the potential strength degradation. To increase the flexibility of dimensions of the cored MRSCs, built-up sections were adopted for both the core (H-section) and side (T-section) segments where the web thickness is set to be equal to the flange thickness, as shown in Fig. 4(b). In the fabrication, the core-segment was first built up through fillet welding (Fig. 4(b)), and the side-segments were then attached to the core-segment by fillet welding before connecting to the end plates by full penetration welding. It should be noted that the thickness of the side-segments, t_s, may be different from that of the core-segment, t_c. The thickness of t_c should be sufficient to prevent shear yielding of the core-segment web under the ultimate shear loads as assuming only the core-segment web resists the shear loads of the member.

The RCS design was adopted on flanges of both the core and side-segments to enlarge the length of plastic-hinges at the ends and therefore member deformation capacity. The adopted shape of the reduced section on the flanges was to match the moment capacity of cross section to the moment demand of the member along the member length, L, within the length of the reduced-section, L_r, assuming the inflection point (zero-moment point) was formed right in the middle of the member, as shown in Fig. 4(a). It should be noted that to achieve the maximum member ductility, the length of L_r in this pilot experimental study was enlarged to the maximum which could be geometrically fitted in specimens considering the feasibility of the fabrication. It resulted in that the smallest width of the flanges in the RCS was about three times of the web thickness of the core-segment. In addition, the ends of the cored MRSC were properly reinforced by several stiffeners and cover plates on both the inner and outer flanges to ensure the plastic hinges were shifted away from the weld connections of end plates as shown in the figure.

The design of cored MRSC was aimed to provide a hysteretic behavior with two plastic strength capacities, i.e. two-phase plastic moment capacities at the critical section as shown in Fig. 4(b), and to form a tri-linear strength backbone curve, as illustrated in Fig. 3 comparing with that of the typical MRSCs. It should be noted that the greater cross-section of the assembly of the core- and side-segments results in the initial stiffness of the member, and the effects of early yielding and greater ductility of the tri-linear strength behavior helps to enlarge the plastic deformation capability as shown in Fig. 3. The first plastic moment capacity, M_{p1}, could be estimated by Eq. (1) below based on the stress distribution of the cross section as the side-segments are fully yielded, and the flange outer surface of the core-segment just reaches the yield strength of steel used for the side-segment, $F_{y,s}$, as depicted in Fig. 5.

$$M_{p1} = F_{y,s}(Z_{x,s} + S_{x,c}) \tag{1}$$

where $Z_{x,s}$ denotes the plastic modulus of those two side-segments assuming plane section remains plane, and $S_{x,c}$ denotes the section modulus of the core-segment. The second plastic moment capacity, M_{p2}, could be estimated by Eq. (2) below based on the stress distribution of the cross

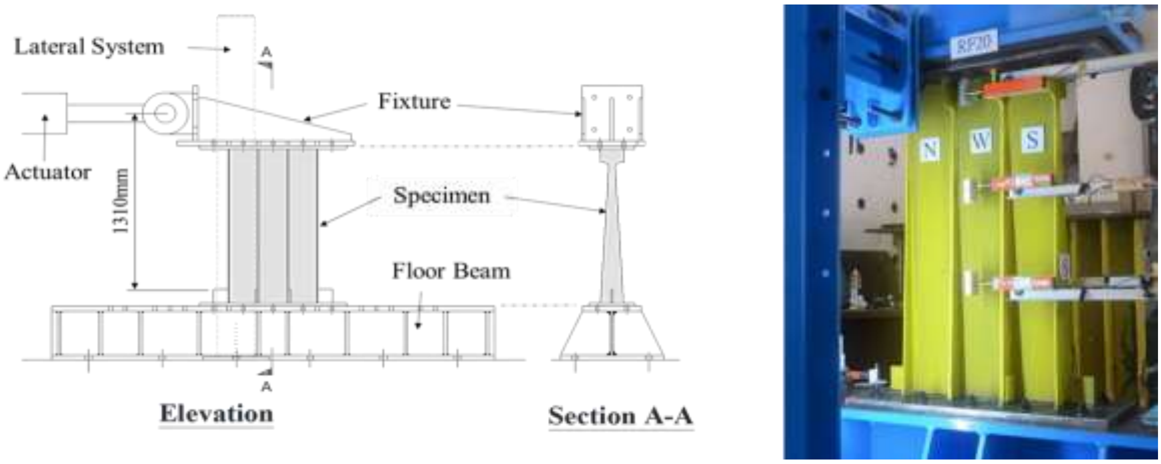

Fig. 6 Elevations and a photo of adopted test setup in the experimental program

Table 1 Adopted cyclic loading protocol

Steps	Story Drift level (%)	Lateral Displacement (mm)	No. of Cycles	Loading Rate (mm/sec)
1	0.1	1.6	2	0.25
2	0.25	4	2	0.25
3	0.5	8	2	0.25
4	1	16	2	0.25
5	1.5	24	2	0.5
6	2	32	2	0.5
7	2.5	40	2	0.5
8	3	48	2	0.5

section as the side-segments are fully yielded and have developed its strain hardening ($C_hF_{y,s}$), the flanges of the core-segment are fully yielded, and the web of the core-segment just reaches its yield strength ($F_{y,c}$), as depicted in Fig. 5.

$$M_{p2} = C_h F_{y,s} Z_{x,s} + F_{y,c}(Z_{x,cf} + S_{x,cw}) \tag{2}$$

where C_h denotes the strain hardening coefficient of the adopted low-yield steel for the side-segments, $Z_{x,cf}$ denotes the plastic modulus of core-segment flanges, and $S_{x,cw}$ denotes the section modulus of core-segment web. Two plastic moment capacities of the critical cross sections mentioned above could be transferred to the corresponding lateral plastic load capacities (or end shear forces) of the member, P_{p1} and P_{p2}, by Eqs. (3) and (4), respectively.

$$P_{p1} = \frac{2M_{p1}}{L} \tag{3}$$

$$P_{p2} = \frac{2M_{p2}}{L} \tag{4}$$

Fig. 3 compares the ideal strength backbone of the proposed cored MRSC and that of the typical MRSC assuming they have the same ultimate load capacities (i.e., P_{p2}). Overall speaking, the development of the cored MRSCs is to achieve (a) greater initial stiffness, (b) greater post-yield stiffness, (c) greater deformation capacity (i.e., overall ductility), (d) larger plastic region (as illustrated in Fig. 3), and (e) reduced strength degradation beyond local buckling of the flanges compared to their counterpart of typical MRSCs.

3. Experimental program

A pilot experimental program has been conducted to examine the proposed cored MRSCs focusing on the mechanism and hysteretic performance of the flexural plastic hinges. Full-scale specimens of the cored MRSC in half, including the end connection and the RCS detailing, were tested assuming the strength-to-deformation behavior of the stub column is symmetric about the inflection point locating right in the mid-height of the stub column. Figure 6 shows the adopted test setup in the study with a photo of an installed specimen. All dimensions of specimens were designed according to a story height of 3.2 m. The specimen was anchored to a floor beam through a bolted end-plate connection as a fixed support. One 490-kN hydraulic actuator was used to apply lateral cyclic loadings at the height of the expected inflection point (the mid-height of

Table 2 Dimensions and material properties of specimens

Specimen	Segment	Steel Grade	F_y (MPa)	F_u (MPa)	Sections (mm)	Height (mm)	d (mm)	b_f/t_f	$\lambda_{hd,f}$	h/t_w	$\lambda_{hd,w}$
RF20	Side	LYS100	135	263	T 198×155×8×8	1145	608	9.69	11.55	23.75	57.37
	Core	SN490B	368	533	H 212×155×12×12			6.46	6.99	15.67	34.72
NRF20	Side	LYS100	135	263	T 198×155×8×8	1145	608	9.69	11.55	23.75	57.37
	Core	SN490B	368	533	H 212×155×12×12			6.46	6.99	15.67	34.72
RF25	Side	LYS100	135	263	T 262×155×8×8	1145	608	9.69	11.55	19.2	57.37
	Core	SN490B	368	533	H 173×155×12×12			6.46	6.99	16.25	34.72
RF15	Side	LYS100	135	263	T 162×155×8×8	1145	608	9.69	11.55	31.75	57.37
	Core	SN490B	368	533	H 223×155×12×12			6.46	6.99	12.42	34.72

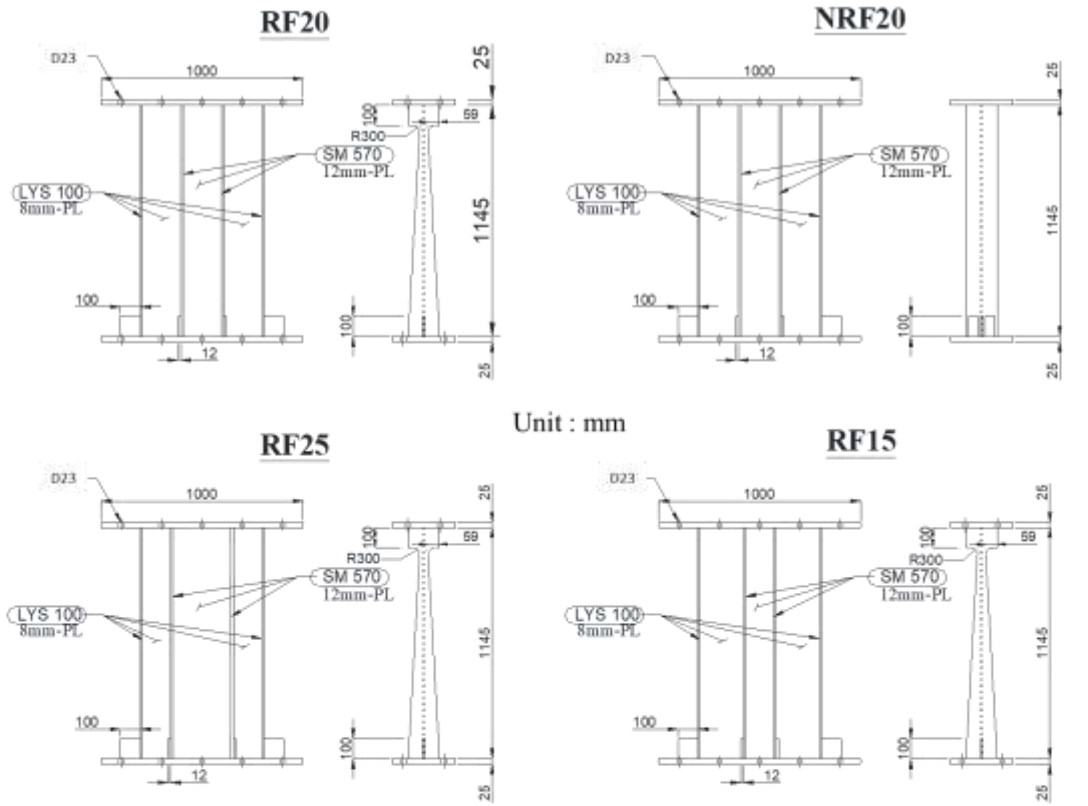

Fig. 7 Detailed dimensions of four specimens in the study

the story). A length of 1310 mm was made between the level of the lateral loads and the critical section of the specimen which was referred to as a half member length (L/2), as defined in Fig. 4(a) and shown in Fig. 6. The applied loads were transferred through a top fixture in the tests when the in-plane and out-of-planer rotations were unconstrained, and a lateral frame system was adopted to prevent out-of-plane displacement at the top of the specimen for a safety concern, as shown in Fig. 6. It should be noted that the out-of-plane instability of the specimen could still be reflected by the out-of-plane rotation of the specimen under the adopted test setup. The cyclic loading protocol from story drift levels of 0.1% to 3.0% radians, as shown in Table 1, was applied followed by fatigue cycles at story drift level of 2.0% or 2.5% radians until the initiation of fracture on the outer flanges. A typical story height of 3.2 m was considered for applying the lateral displacements according to the interstory drifts in the tests, as listed in Table 1. Two cycles were applied at each story drift level to identify the strength degradation of the specimens, if any.

3.1 Design of specimens

Four full-scale specimens of one-half cored MRSC members were tested in the study. Table 2 presents the major dimensions and measured material properties based on tensile tests of materials for each specimen, including yield (F_y) and tensile strengths (F_u). LYS100 steel grade was adopted for the side-segments, while SN490B steel grade was used for the core-segments in each specimen. The overall height and depth of each specimen are 1145 and 608 mm, respectively. Various depths of the side and core-segments were experimentally examined and compared among specimens. The flange and web dimensions of each specimen were selected to meet the seismic compact sections per AISC seismic provisions (AISC 341-10). The adopted flange and web slenderness ratios, b_f/t_f and h/t_w, are shown in Table 2 compared with the specified limits of the slenderness ratios, i.e., $\lambda_{hd,f}$ and $\lambda_{hd,w}$ which represent the limits for flanges and webs respectively per the design code. RF20 was a baseline specimen in which the depth of the core-segment (H-section) was similar with that of the side-segments (T-section). 8 mm- and 12 mm-thick plates were used for the side and core-segments, respectively. NRF20 was the counterpart specimen, which had identical dimensions with RF20 but no details of the RCS, to verify the effect of the RCSs. Furthermore, specimens RF25 and RF15 were similar with the baseline but having deeper and shallower core-segments, respectively, as the overall depths remain the same. More detailed dimensions of each specimen are given in Fig. 7 with the details of the RCSs and reinforced connection at the bottom end. The reduced section was applied on flanges of both the side- and core-segments in a triangular shape as shown, which is determined by making the moment of inertia of the cross section vary with the moment demands along the member length (L). It should be noted that the length L_r was enlarged in this pilot study to examine the maximum lateral deformation capacity of the cored MRSC when not satisfying the requirements of preventing lateral torsional buckling (LTB) per design code (AISC 360-10) considering the presence of the lateral support in the test setup. Several stiffeners and cover plates were added on the flanges of both the side- and core-segments to ensure the plastic hinge region to be shifted away from the welding connection at the end-plate, as shown in Fig. 7.

3.2 Test observations and measured responses

The measured hysteretic responses of all specimens are shown in Fig. 8. With the presence of the core-segment, four specimens all provided a stable cyclic behavior with very neglectable strength degradation by the end of the increasing-amplitude cyclic loading, and relatively large post-yielding stiffness beyond the first lateral plastic load capacity (P_{p1}). Various initial elastic stiffness, post-yield stiffness, and lateral plastic load capacities were shown among specimens due to the variation of the depth of the core-segment and the adoption of the RCS detailing. An additional parametric study was performed to develop estimation equations of the stiffness at various deformation levels as presented later in the study.

Upon the test observations, the specimens started yielding prior to the story drift of 0.5% radians on the side-segment. Fig. 9 compares the photos of four specimens which were taken in the cycles at the 1.5% story drift level. It is shown that the specimens with the RCS detailing, i.e., RF20, RF25 and RF15, had more distributed yielding throughout entire length of L_r on the side-segment compared to NRF20 where the yielding area concentrated only in the lower portion of the side-segments, while the core-segment mostly remained elastic in all specimens. It is verified that the plastic region could be enlarged by adopting the detailing of the RCS. Except the yield mechanism, several failure modes were observed in the tests including local buckling (LB), out-of-plane rotation (OR), side-segment buckling (SSB), and fracture (F) on the side-segment flanges in sequences, as shown in Fig. 10. The occurrences of those failure modes during the tests are labelled in the measured hysteretic loops as shown in Fig. 8 based on the test observations. The shown lateral plastic load capacities (P_{p1} and P_{p2}) of each specimen in the figures were calculated based on Eqs. (1)-(4) according to the cross-sectional dimensions of the critical sections, as shown in Table 3. It should be noted that the flange widths of NRF20 at the critical sections were slightly larger than others with RCS detailing. It is shown that those equations (Eqs. (1)-(4)) enabled to represent the measured lateral plastic load capacities of the test responses.

All specimens presented a very stable hysteretic behavior without any strength degradation prior to the LB of the side-segment flanges around the critical section. The LB occurred in the cycles of 1.0% story drift for NRF20 and RF15, while in the cycles of 1.5% story drift for RF20 and RF25. It was shown that both adopting the RCS detailing and a decrease of the side-segment depth would help to delay the occurrence of LB. The OR was observed in the specimens with RCS after the occurrence of the LB as shown in Figs. 8 and 10. The OR behavior was caused by the insufficient out-of-plane rotational stiffness at the top end of the RCS region due to a small weak-axis moment of inertia of the cross section. The OR was observed more severe under the positive displacement of the actuator due to the adopted loading setup that caused a reduction on the measured strengths, and gradually increased with the applied story drifts as shown. It thereby resulted in an asymmetrical hysteretic responses of the specimen.

The SSB behavior (Fig. 10) was observed in the specimen with RCSs due to the severe yield of entire length of the side-segments after the occurrence of the LB and OR mentioned in the relatively large story drift cycles. Moderate strength degradation was observed after the occurrence of the SSB which is referred to that the core-segment remained mostly elastic and unbuckled and formed a strong-back portion in the member to minimize the deformation concentrations. Bolt shear failure (BSF) of a single bolt was observed at the bottom end-plate connection in the first cycle of 2.5% story drift in NRF20 and NR25 and therefore terminated the increase amplitude loading, as shown in Fig. 8. The BSF occurred solely under negative displacement of the actuator since the strengths under positive displacement of the actuator were smaller due to the OR mentioned above. It should be noted that the OR and SSB mentioned above are undesired failure modes which are expected to be eliminated by ensuring enough weak-axis radius of gyration of the critical section and

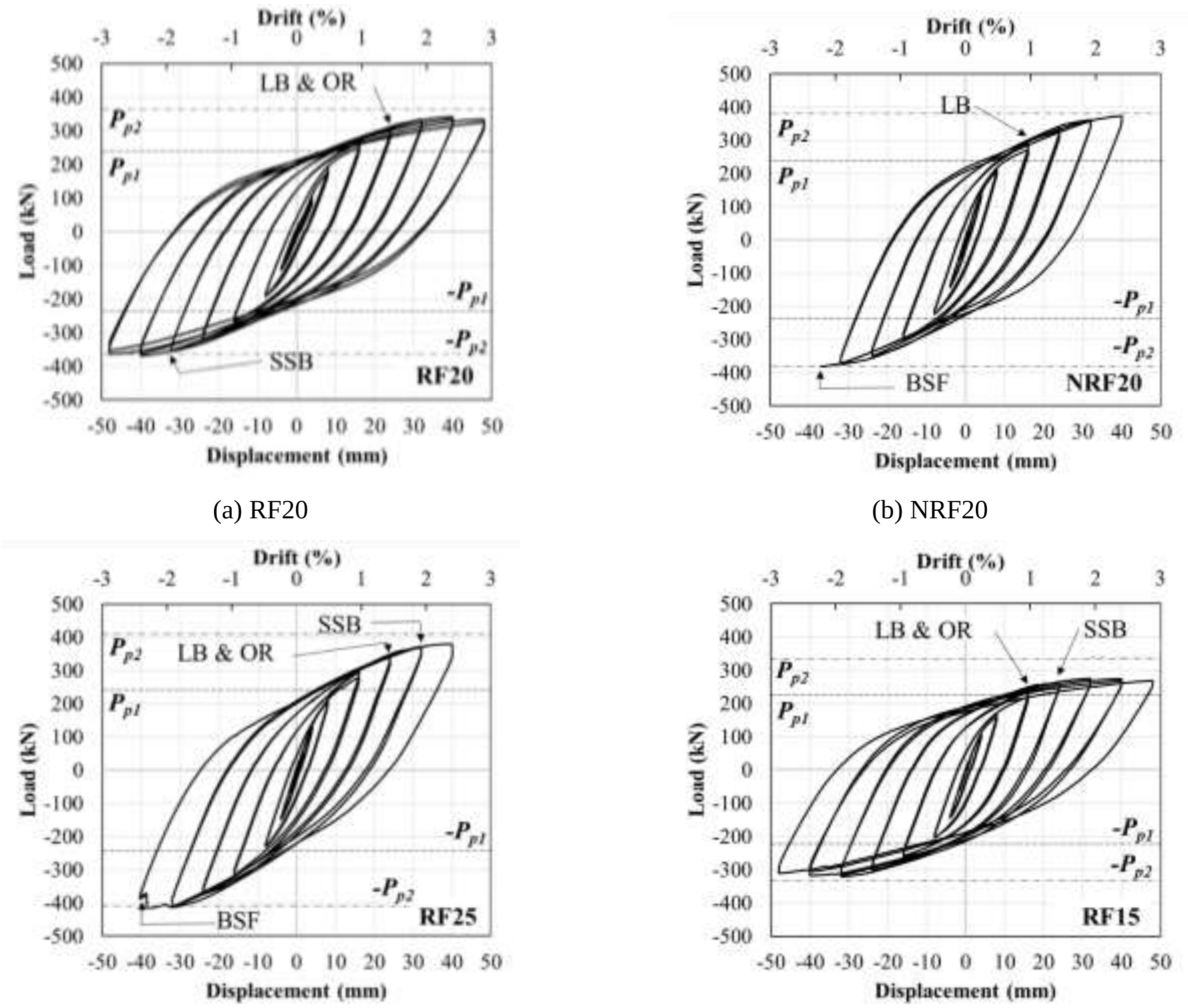

(a) RF20 (b) NRF20

(c) RF25 (d) RF15

Fig. 8 Measured hysteretic responses and observed failure modes in the increasing amplitude cycles

Table 3 Estimated lateral plastic load capacities (P_{p1} and P_{p2}) of each specimen

Specimen	M_{p1} (kN-m)	M_{p2} (kN-m)	$L/2$ (mm)	P_{p1} (kN)	P_{p2} (kN)	Δ_{p1} (mm)
RF20	228	364	1310	174	278	9
NRF20	239	382	1310	182	292	8
RF25	239	403	1310	182	308	8
RF15	217	326	1310	166	249	8

shortening the length of L_r, respectively. Further experimental research is still needed to experimentally verify the limits. It should be stated that further experimental research of testing whole SC components is still needed to clarify the limits of the length L_r to ensure the lateral stability of the cored MRSCs.

To examine the fatigue lives of the specimens, fatigue cycles at 2% story drift level were continuously applied to the specimens with RCSs after the increase amplitude cycles. A total of 26 cycles were completed in the fatigue test of RF20 prior to observed fracture (F) at the side-segment flange around the critical section (Fig. 11(a)), while only 10 cycles were completed in the fatigue test of RF25 prior to the fracture (Fig. 11(b)). It should be noted that the fracture observed here did not lead to a total loss of the overall strength of the member due to the presence of the elastic core-segment. RF15 presented the most ductile behavior in the study that no fracture was observed before the termination of the test after a completion of 50 cycles (Fig. 11(c)).

Fig. 9 Photos of specimens during the cycles of 1.5% story drift

Fig. 10 Photos of observed failure modes of the specimens

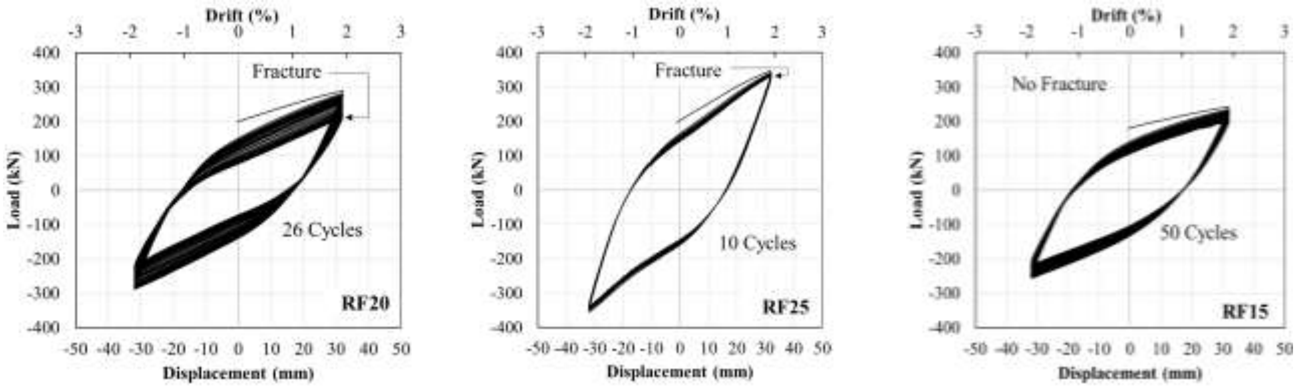

(a) RF20 (b) RF25 (c) RF15

Fig. 11 Measured hysteretic responses in the fatigue cycles

3.3 Cumulative plastic deformations and energy dissipation

Based on the measured results, the fatigue live of each specimen was evaluated through the cumulative plastic deformation (CPD) and energy dissipations. The CPD values are defined and calculated following Eq. (5).

$$\mathrm{CPD} = \frac{\sum \Delta_p}{\Delta_{p1}} \quad (5)$$

where $\Sigma\Delta_p$ denotes the cumulative plastic deformation. Δ_{p1} denotes the deformation corresponding to the first lateral plastic load capacities (P_{p1}) as illustrated in Fig. 3, and the

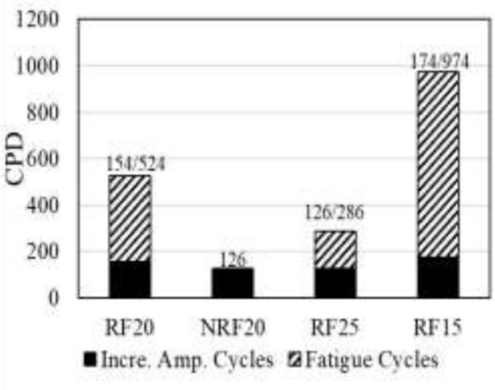

(a) CPD

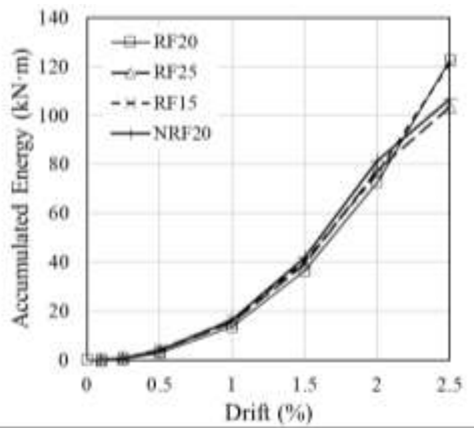

(b) Cumulative energy dissipation

Fig. 12 The measured cumulative ductility and energy dissipation of specimens

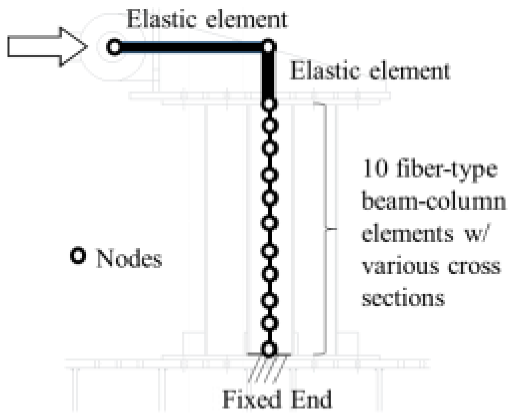

Fig. 13 Illustration of the adopted discrete model of specimens

measured values of Δ_{p1} are listed in Table 3. The resulting CPDs including both the increase-amplitude and fatigue cycles for each specimen are shown in Fig. 12(a). The baseline specimen (RF20) achieved a CPD value of 524, while the CPD of the specimen with deeper core-segment (RF25) reduced around 45%. The specimen with shallower core-segment (RF15) enables to achieve a CPD of at least 974 since no fracture was found by the end of the tests. It should be noted that the shown values of the CPD here provide a lower bound of the fatigue live for each specimen considering that the fatigue live would be further extended if the failure modes of the OR and SSB are prevented.

The cumulative energy dissipation of each specimen was calculated by integrating the areas enclosed by the measured hysteretic loops for all completed cycles. The resulting cumulative energy dissipations of each specimen at each story drift levels up to 2.5% story drift are shown in Fig. 12(b). The results of all specimens were very similar to each other. Relatively lower energy dissipations were found in NRF20 and NF25 since only one cycle at 2.5%story drift level was completed in the tests as mentioned previously. It should be noted that all experimental findings mentioned above on the seismic performance of the MRSC were based on four pilot tests with various conditions in the study. More experimental work is still needed to verify or further improve the results concluded in the study.

4. Numerical simulations

A general discrete model was developed in OpenSees frameworks (Mazzoni *et al.* 2006) to simulate the nonlinear behavior of the cored MRSCs. The developed model was first validated by the experimental results before adopted for a parametric study in the study. Fig. 13 illustrates the proposed discrete model adopted for the specimens. Ten fiber-type nonlinear beam-column elements with various cross sections were adopted to simulate the specimen with the RCS, while two elastic elements with relatively large elastic modulus were used to simulate the rigidity of the top fixture. Different material properties were assigned to the core- and side-segments on each fiber section using Steel02 material model. The measured properties of steels upon tensile tests, as listed in Table 2, were adopted in the analyses. Assuming the floor beam is fully rigid, the bottom end was fully restrained as a fixed end in the simulation, and a free end was adopted at the loading point. The elements simulating the top fixture were restrained from

Table 4 The major parameters of samples in the parametric study

Cases	d (mm)	b_f (mm)	L (mm)	d_c/d (mm)	t_c (mm)	t_s (mm)	$2L_r/L$ (mm)
Case 0	700	150	2620	0.33	24	16	0.4
Case 1	300	150	2620	0.33	24	16	0.4
Case 2	500	150	2620	0.33	24	16	0.4
Case 3	900	150	2620	0.33	24	16	0.4
Case 4	1100	150	2620	0.33	24	16	0.4
Case 5	1300	150	2620	0.33	24	16	0.4
Case 6	700	110	2620	0.33	24	16	0.4
Case 7	700	200	2620	0.33	24	16	0.4
Case 8	700	250	2620	0.33	24	16	0.4
Case 9	700	300	2620	0.33	24	16	0.4
Case 10	700	150	2620	0.25	24	16	0.4
Case 11	700	150	2620	0.5	24	16	0.4
Case 12	700	150	2620	0.75	24	16	0.4
Case 13	700	150	2620	0.33	12	16	0.4
Case 14	700	150	2620	0.33	16	16	0.4
Case 15	700	150	2620	0.33	20	16	0.4
Case 16	700	150	2620	0.33	24	8	0.4
Case 17	700	150	2620	0.33	24	12	0.4
Case 18	700	150	2620	0.33	24	20	0.4
Case 19	700	150	2620	0.33	24	24	0.4
Case 20	700	150	1784	0.33	24	16	0.4
Case 21	700	150	2202	0.33	24	16	0.4
Case 22	700	150	3038	0.33	24	16	0.4
Case 23	700	150	3456	0.33	24	16	0.4
Case 24	700	150	2620	0.33	24	16	0.48
Case 25	700	150	2620	0.33	24	16	0.32
Case 26	700	150	2620	0.33	24	16	0.16

out-of-plane deformations. Measured deformations of the cyclic loading of each specimen until the story drift of 2.5% radians upon the test results were applied in the analyses. The resulting analytical results of each specimen are shown in Fig. 14 comparing with the experimental responses. It is shown that numerical model enables to accurately capture the hysteretic behaviors of specimens, including initial stiffness, post-yield stiffness, unloading stiffness and strength backbones. It should be noted that the fiber-type discrete model is under the assumption that plane section remains plane and therefore unable to capture the behaviors of LB, OR and SSB observed in the tests. In consequence, no strength degradations and more symmetric hysteretic behavior were shown in the analytical results. However, it was verified that the developed numerical model enabled to accurately capture the hysteretic behavior of the cored MRSCs prior to the occurrence of the OR and SSB.

5. Parametric analytical study

A parametric analytical study was performed using the developed numerical model mentioned above to establish the equations of estimating the strength backbones, including the initial and post-yield stiffness, of the cored MRSCs which is difficult to estimate due to the complex geometries and mechanism. A wide range of dimensions of the member was included in the parametric study to comprise the most range in the real applications, as listed in Table 4. A total of 27 cases were considered among which not only the major dimensions (d, b_f, L, t_c and t_s) but also the depth and length ratios (d_c/d and $2L_r/L$) were varied as shown in Table 4 and Figs. 4(a) and 4(b). The sizes of d varied from 300 to 1300 mm, the sizes of b_f varied from 110 to 300 mm, and the overall length (L) varied from 1784 to 3456 mm. The values of t_c varied from 12 to 24 mm, while the values of t_s varied from 8 to 16 mm.

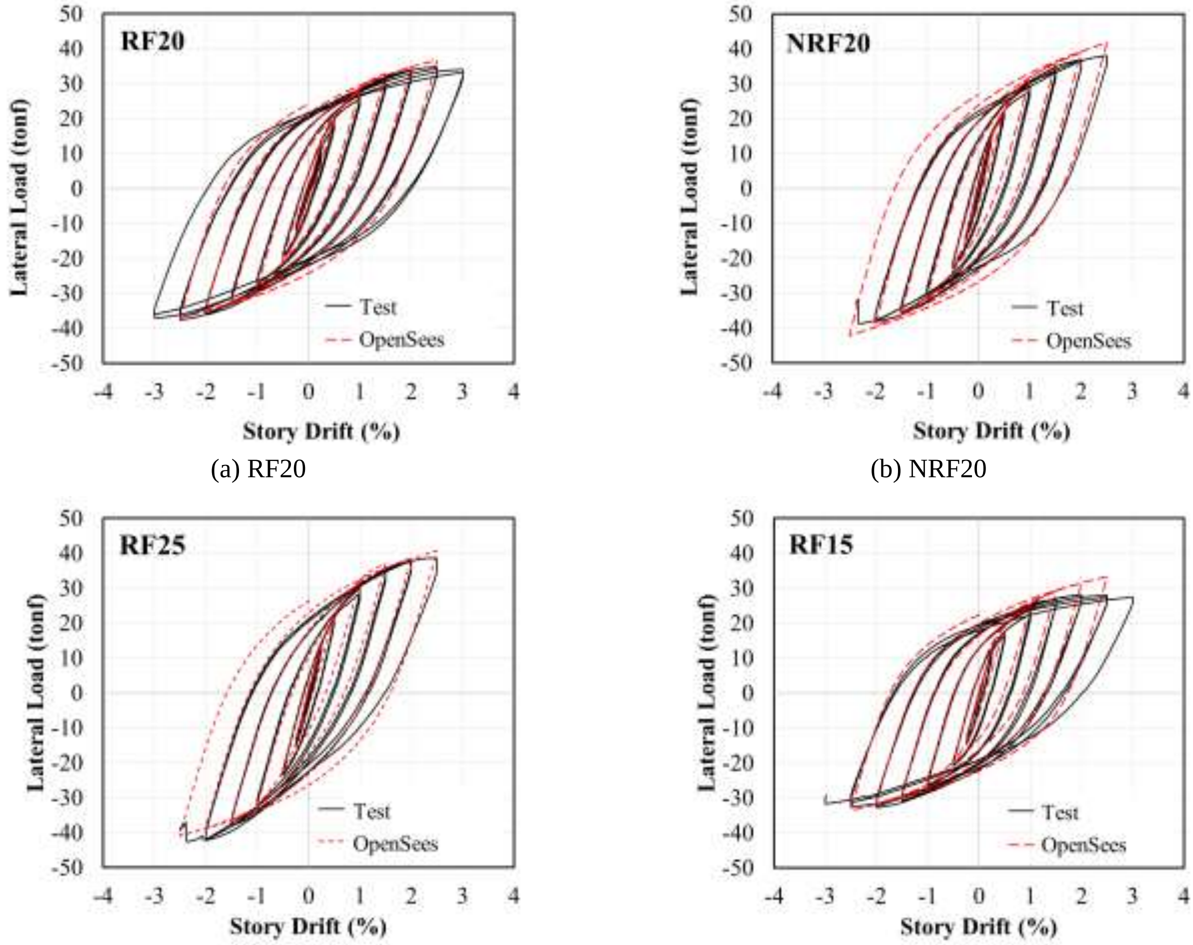

(a) RF20 (b) NRF20

(c) RF25 (d) RF15

Fig. 14 Comparisons of measured and analytical hysteretic responses of specimens

The various member sizes (d, b_f) were selected by following the typical use of SCs in the real applications, and various member lengths (L) was included to consider various story heights in the real practice. The web and flange slenderness ratios in each case were selected to satisfy the seismic compact sections per AISC seismic provisions (AISC 341-10). Moreover, the ratios of d_c/d varying from 0.25 to 0.75 were considered to cover the most situations. The ratios of $2L_r/L$ varying from 0.16 to 0.48 in which the weak-axis radiuses of gyration (r_y) of the smallest cross section within the RCS were sufficient to prevent LTB behavior following Eq. (6) per AISC specification (AISC 360-10) to conservatively prevent the failure modes of OR and SSB observed in the experiments.

$$L_p = 1.76 r_y \sqrt{\frac{E}{F_y}} \tag{6}$$

where E denotes the elastic modulus of steel (200 GPa). The L_p and F_y are considered as the member length (L) and the nominal yield strength of the side-segment flanges, respectively.

All cases considered in the study were individually analyzed using the developed modelling approach mentioned above in OpenSees framework (Mazzoni et al. 2006). A gradually increase-amplitude cyclic loading was applied in the analyses from story drifts of 0.125% to 2.5% radians with an interval of 0.125% story drift where only one cycle was applied at each drift level. Figure 15 shows an example of the resulting analytical hysteretic responses in the study. A strength backbone curve (as shown in bold line) was first obtained for each case, as illustrated in the figure. The analytical strengths ($P_{p1,ana}$ and $P_{p2,ana}$) and stiffness ($K_{1,ana}$ and $K_{2,ana}$) were then obtained based on the tri-linear curve formed by the tangents of the strength backbone as shown in Fig. 15. Figures 16(a)-(b) compare the resulting values of obtained $P_{p1,ana}$ and $P_{p2,ana}$ with the results calculated by Eqs. (1)-(4) above which are denoted to as $P_{p1,cal}$ and $P_{p2,cal}$, respectively. A good agreement was shown between the analytical and calculated results with errors within +/-10%. It was verified that Eqs. (1)-(4) could successfully estimate the lateral plastic loads (P_{p1} and P_{p2}) of the cored MRSCs with a good accuracy.

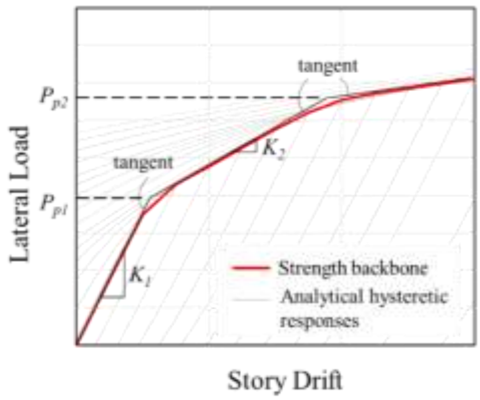

Fig. 15 Illustration of the method of obtaining stiffness and plastic strength capacities upon analytical results

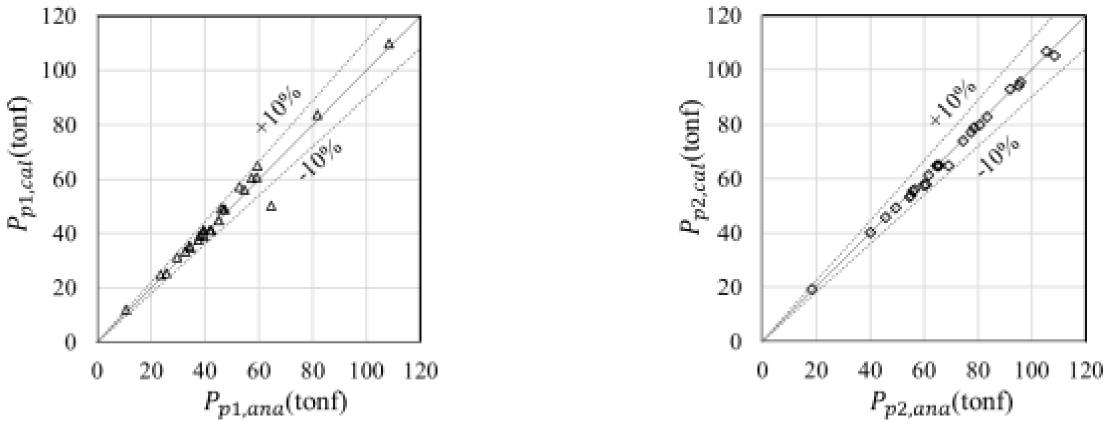

(a) P_{p1}

(b) P_{p2}

Fig. 16 Comparisons of calculated and analytical lateral plastic load capacities

Regression analyses were performed to establish the empirical equations of estimating the initial stiffness (K_1) and the post-yield stiffness (K_2) individually based on the analytical responses in the parametric study. The regression equations are upon the slenderness ratios (L/r_{gx}) and two non-dimensional geometric parameters of $2L_r/L$ and d_c/d as shown, and the typical elastic stiffness term of the member without the RCS detailing ($12EI_{gx}/L^3$) is also included in the formulae. Where I_{gx} and r_{gx} denote the moment of inertia and the radius of gyration of the gross cross section of the critical section with respect to the strong axis of the section, *x-x axis*, as shown in Fig. 4(b). Eqs, (7) and (8) show the regression results for the initial stiffness (K_1) and the post-yield stiffness (K_2) in the SI unit of tonf/mm, respectively.

$$K_1 = 0.13\left(\frac{12EI_{gx}}{L^3}\right)\left(\frac{L}{r_{gx}}\right)^{0.83}\left(\frac{2L_r}{L}\right)^{-0.08}\left(\frac{d_c}{d}\right)^{0.39} \quad (7)$$

$$K_2 = 0.24\left(\frac{12EI_{gx}}{L^3}\right)\left(\frac{L}{r_{gx}}\right)^{0.39}\left(\frac{2L_r}{L}\right)^{-0.23}\left(\frac{d_c}{d}\right)^{1.33} \quad (8)$$

Figs. 17(a) and 7(b) present the accuracy of the calculated results of the stiffness ($K_{1,cal}$ and $K_{2,cal}$) with respect to the analytical results ($K_{1,ana}$ and $K_{2,ana}$). It was shown that Eq. (7) provided an accurate estimation of the initial stiffness (K_1) with errors within +/-10%, while Eq. (8) gave a fair accuracy of estimating the post-yield stiffness (K_2) with errors within +/-30%. Figures 18(a)-(b) compare the analytical and calculated stiffness (K_1 and K_2) with respect to the member slenderness (L/r_{gx}), while Figs. 18(c) and 18(d) compare that with respect to the member slenderness typical elastic stiffness of the member without RCS detailing ($12EI_{gx}/L^3$). It was shown that the cases in the study cover a wide range of member slenderness (from 6 to 29) and initial stiffness (from 2 to 67 tonf/mm). The values of the stiffness reduced with the increase of the member slenderness which is similar with the typical MRSC member. It was also shown that the stiffness increased proportionally with the increase of the term of $12EI_{gx}/L^3$ approximately in a linear trend. The comparisons shown in Fig. 18 verify that the proposed formulae (Eqs. (7) and (8)) provided more accurate estimations of the stiffness, which reflects the geometry of the RCSs, compared to the prediction solely based on either member slenderness or the term of $12EI_{gx}/L^3$.

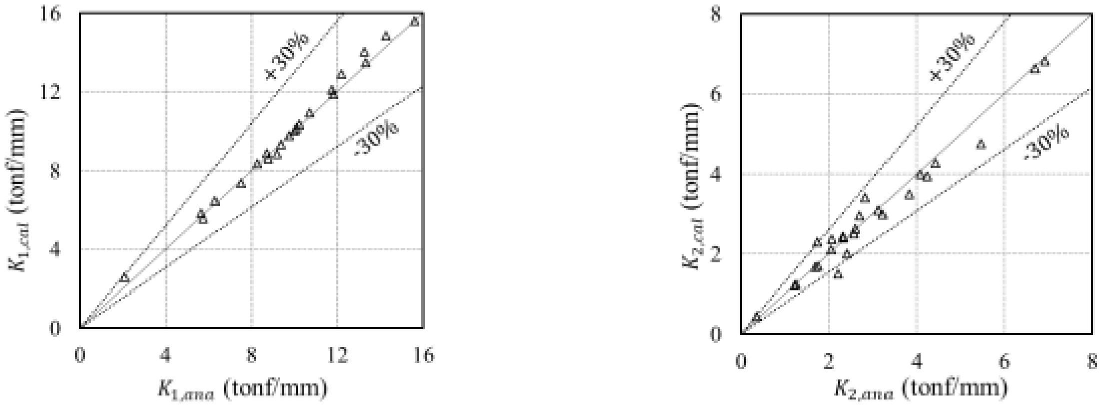

(a) k_1 (b) $k2$

Fig. 17 Comparisons of calculated and analytical values of the stiffness

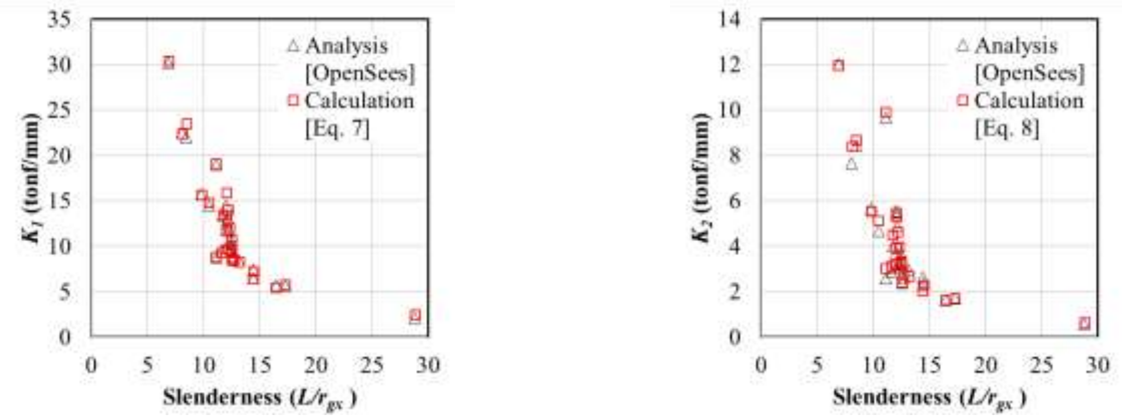

(a) K_1 vs. Slenderness (b) K_2 vs. Slenderness

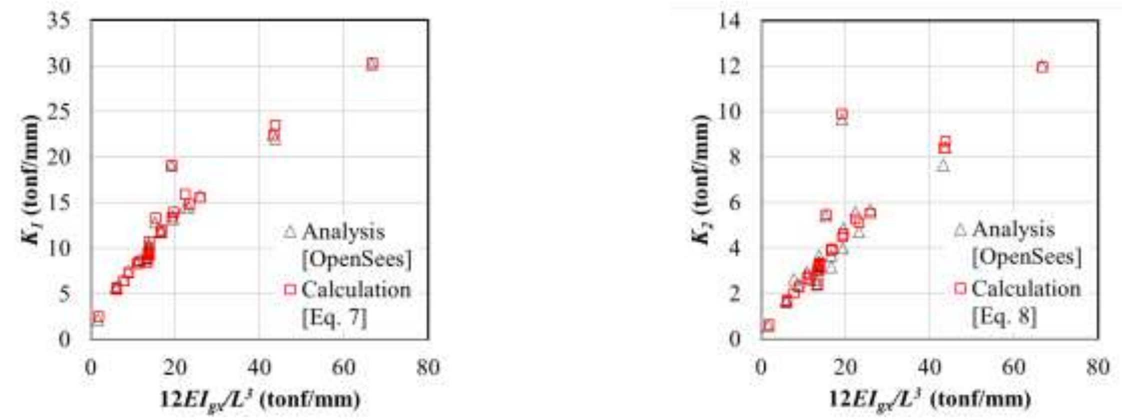

(c) K_1 vs. ($12EI_{gx}/L^3$) (d) K_2 vs. ($12EI_{gx}/L^3$)

Fig. 18 Comparisons of calculated and analytical results of the stiffness versus member slenderness and typical elastic stiffness of the member without RCS detailing

Furthermore, the story drifts (Δ_{p1} and Δ_{p2}) corresponding to the lateral plastic load capacities (P_{p1} and P_{p2}) as shown in Fig. 3 could be obtained based on the results of P_{p1}, P_{p2}, K_1 and K_2 (Eqs. (1)-(4), (7)-(8)). The developed equation-based estimation method in the study forms an essential basis for developing the design procedure of the proposed cored MRSCs as one of the future work.

6. Conclusions

A design of the cored MRSC has been newly developed and proposed in the study to form a ductile hysteretic behavior with features of early yielding, greater post-yield stiffness and reduced strength degradation compared with typical MRSCs. Four full-scale specimens of one-half cored MRSCs had been tested focusing on the seismic performance of flexural plastic hinges at the ends of the member. The increasing-amplitude cyclic loadings followed by fatigue cycles were applied to experimentally examine the specimens. The effects of the depths of the core-segment and the detailing of the RCS on the hysteretic behavior of specimens were investigated. In addition, a numerical modelling approach was developed for the cored MRSCs and validated by the measured responses of the tests. The developed numerical model was then adopted to perform a parametric study for the cored MRSCs. Finally, an equation-based estimation method of the strength backbone of the cored MRSCs was established and validated upon the results of the parametric study. Some conclusions are made in the study as listed below:

- The mechanics of the proposed cored MRSCs has been experimentally verified. It was shown that the side-segments enabled to provide early yielding and significant energy dissipation, while the core-segment mostly remained elastic and thereby enhanced the post-yield stiffness and limited strength degradation of the member due to flange local buckling of the side-segments.
- The effect of adopting RCS details at the ends of the cored MRSCs was verified to extend the plastic hinge region on the side-segments which potentially enlarge the deformation capacity of the member. However, the undesired failure modes of OR and SSB were caused by the out-of-plane instability due to the overlong RCSs adopted in the tests. The lengths of RCSs are suggested to be determined by checking on the member stability to prevent LTB failure of the member.
- The effect of the core-segment depth was experimentally clarified. Deeper core-segment was found to enhance overall stiffness and strengths of the member but reduce CPDs. In contrast, the member with shallower core-segment provided lower overall stiffness and strengths but significantly increases its CPD values.
- A general discrete model was established for the cored MRSCs, which was validated by the measured results in the study and enabled to accurately simulate the seismic performance of the cored MRSCs.
- Some physical model equations of estimating the lateral plastic load capacities (P_{p1} and P_{p2}) were developed and validated by the measured results and the developed numerical model in the study.
- A set of regression equations was developed to accurately estimate the initial and post-yield stiffness (K_1 and K_2) of the cored MRSCs based on the results of the parametric study using the developed discrete model and considering a wide range of member dimensions. An equation-based estimation method of the strength backbone of the cored MRSCs was finally established which is an essential basis for developing design procedures of the cored-MRSCs as one of the future work in the study.

Acknowledgements

Ministry of Science and Technology, R.O.C. and National Taiwan University of Science and Technology are gratefully acknowledged for financing and supporting the project under the Grants MOST106-2625-M-005-003.

References

AISC 341-10 (2010), Seismic Provisions for Structural Steel Buildings, American Institute of Steel Construction; Chicago, Illinois, USA.

AISC 360-10 (2010), Specification for Structural Steel Buildings, American Institute of Steel Construction; Chicago, Illinois, USA.

Alfredo, R.S., Manuel, E.S.L., José, R.G.C., Edén, B. and Arturo, L.B. (2014), "Seismic response estimation of steel buildings with deep columns and PMRF", *Steel Compos. Struct.*, **17**(4), 471-495. http://dx.doi.org/10.12989/scs.2014.17.4.471.

Dehghan, S.M., Najafgholipour, M.A., Ziarati, S.M. and Mehrpour, M.R. (2018), "Experimental and numerical assessment of beam-column connection in steel moment-resisting frames with built-up double-I column", *Steel Compos. Struct.*, **26**(3), 315-328. http://dx.doi.org/10.12989/scs.2018.26.3.315.

Deng, K., Pan, P., Li, W. and Xue, Y. (2015), "Development of a buckling restrained shear panel damper", *J. Constr. Steel Res.*, **106**, 311-321. https://doi.org/10.1016/j.jcsr.2015.01.004.

Elkady, A. and Lignos, D.G. (2015), "Analytical investigation of the cyclic behavior and plastic hinge formation in deep wide-flange steel beam-columns", *Bull. Earthq. Eng.*, **13**, 1097-1118. https://doi.org/10.1007/s10518-014-9640-y.

Engelhardt, M.D. and Popov, E.P. (1992), "Experimental performance of long links in eccentrically braced frames", *J. Struct.Eng.*, **118**(11), 3067-3088. https://doi.org/10.1061/(ASCE)0733-9445(1992)118:11(3067).

He, L., Kurata, M. and Nakashima, M. (2015), "Condition assessment of steel shear walls with tapered links under various loadings", *Earthq. Struct.*, **9**(4), 767-788. https://doi.org/10.12989/eas.2015.9.4.767.

Hsiao, P.C. and Liao, W.C. (2019), "Effects of hysteretic properties of stud-type dampers on seismic performance of steel moment resisting frame buildings", *J. Struct.Eng.-ASCE*, **145**(7). https://doi.org/10.1061/(ASCE)ST.1943-541X.0002346.

Jones, S.L., Fry, G.T. and Engelhardt, M.D. (2002), "Experimental evaluation of cyclically loaded reduced beam section moment connections", *J. Struct.Eng.-ASCE*, **128**(4), 441-451. https://doi.org/10.1061/(ASCE)0733-9445(2002)128:4(441).

Kim, J., Kim, M. and Eldin, M.N. (2017), "Optimal distribution of steel plate slit dampers for seismic retrofit of structures", *Steel Compos. Struct.*, **25**(4), 473-484. http://dx.doi.org/10.12989/scs.2017.25.4.315.

Lian, M., Zhang, H., Cheng, Q. and Su, M. (2019), "Finite element analysis for the seismic performance of steel frame-tube structures with replaceable shear links", *Steel Compos. Struct.*, **30**(4), 365-382. http://dx.doi.org/10.12989/scs.2019.30.4.365.

Lu, L., Xu, Y., Liu, J. and Lim, J.B. (2018), "Cyclic performance and design recommendations of a novel weak-axis reduced beam section connection", *Steel Compos. Struct.*, **27**(3), 337-353. http://dx.doi.org/10.12989/scs.2018.27.3.471.

Mazzoni, S., McKenna, F., Scott, M.H. and Fenves, G. (2006), OpenSees command language manual, 264, Pacific Earthquake Engineering Research (PEER) Center.

Nakashima, M. (1995), "Strain-hardening behavior of shear panels made of low-yield steel. I: Test", *J. Struct. Eng.*, **121**(12), 1742-1749. https://doi.org/10.1061/(ASCE)0733-

9445(1995)121:12(1742).

Richards, P.W. and Uang, C.M. (2005), "Effect of flange width-thickness ratio on eccentrically braced frames link cyclic rotation capacity", *J. Struct.Eng.-ASCE*, **131**(10), 1546-1552. https://doi.org/10.1061/(ASCE)0733-9445(2005)131:10(1546).

Shayanfar, M.A., Barkhordari, M.A. and Rezaeian, A.R. (2012), "Experimental study of cyclic behavior of composite vertical shear link in eccentrically braced frames", *Steel Compos. Struct.*, **12**(1), 13-29. http://dx.doi.org/10.12989/scs.2012.12.1.13.

Soltani, N., Abedi, K., Poursha, M. and Golabi, H. (2017), "An investigation of seismic parameters of low yield strength steel plate shear walls", *Earthq. Struct.*, **12**(6), 713-723. https://doi.org/10.12989/eas.2017.12.5.713.

Tsai, K.C., Wu, S. and Popov, E.P. (1995), "Experimental performance of seismic steel beam-column moment joints", *J. Struct. Eng.*, **121**(6), 925-931. https://doi.org/10.1061/(ASCE)0733-9445(1995)121:6(925).

Uang, C.M. and Fan, C.C. (2001), "Cyclic stability criteria for steel moment connections with reduced beam section", *J. Struct.Eng.-ASCE*, **127**(9), 1021-1027. https://doi.org/10.1061/(ASCE)0733-9445(2001)127:9(1021).

Ye, L.P., Lu, X.Z., Ma, Q.L., Cheng, G.Y., Song, S.Y., Miao, Z.W. and Pan P. (2008), "Study on the influence of post-yielding stiffness to the seismic response of building structures", *Proceedings of the 14th World Conf. on Earthquake Engineering*, China Earthquake Administration Ministry of Construction, Beijing.

Zahrai, S.M. (2015), "Cyclic testing of chevron braced steel frames with IPE shear panels", *Steel Compos. Struct.*, **19**(5), 1167-1184. http://dx.doi.org/10.12989/scs.2015.19.5.471.

Zahrai, S.M., Mirghaderi, S.R. and Saleh A. (2017), "Increasing plastic hinge length using two pipes in a proposed web reduced beam section" , *Steel Compos. Struct.*, **23**(4), 421-433. http://dx.doi.org/10.12989/scs.2017.23.4.421.

BU